Slow slip events are regular earthquakes

Huihui Weng (qfkq7850@mail.ustc.edu.cn)
UCA https://orcid.org/0000-0002-2936-2342

Physical Sciences - Article

Keywords: slow slip events, earthquakes, seismogenic zones

Posted Date: May 27th, 2021

DOI: https://doi.org/10.21203/rs.3.rs-448196/v1

Slow slip events are regular earthquakes

Huihui Weng[1*]

[1] *Université Côte d'Azur, IRD, CNRS, Observatoire de la Côte d'Azur, Géoazur, 250 rue Albert Einstein, Sophia Antipolis, 06560 Valbonne, France*

Correspondence to Huihui Weng (email: weng@geoazur.unice.fr)

Slow slip events usually occur downdip of seismogenic zones in subduction megathrusts and crustal faults, with rupture speeds much slower than earthquakes. The empirical moment-duration scaling relation can help constrain the physical mechanism of slow slip events, yet it is still debated whether this scaling is linear or cubic and a fundamental model unifying slow slip events and earthquakes is still lacking. Here I present numerical simulations that show that slow slip events are regular earthquakes with negligible dynamic-wave effects. A continuum of rupture speeds, from arbitrarily-slow speeds up to the S-wave speed, is primarily controlled by the stress drop and a transition slip rate above which the fault friction transitions from rate-weakening behaviour to rate-strengthening behaviour. This continuum includes tsunami earthquakes, whose rupture speeds are about one-third of the S-wave speed. These numerical simulation results are predicted by the three-dimensional theory of dynamic fracture mechanics of elongated ruptures. This fundamental model unifies slow slip events and earthquakes, reconciles the observed moment-duration scaling relations, and opens new avenues for understanding earthquakes through investigations of the kinematics and dynamics of frequently occurring slow slip events.

Slow slip events (SSEs) have been widely observed downdip of seismogenic zones in subduction megathrusts worldwide and in crustal faults[1–9], and possibly trigger large megathrust earthquakes[10–13], therefore understanding the physical mechanisms of SSEs is of increasing importance. SSEs usually occur in an elongated section of the deep plate interface with rupture speeds much slower than megathrust earthquakes whose ruptures are also elongated (Figure 1a). Earthquake ruptures on elongated faults can steadily propagate at speeds from slower than S-wave up to P-wave speed, depending on the balance between dissipated and potential energies[14]. SSE ruptures can also steadily propagate on elongated faults[15–17], facilitated by a frictional transition from rate-weakening at slow slip rates to rate-strengthening at high slip rates that has been observed experimentally[18–28]. It has been reported that rupture speeds, on a continuum from SSE speeds up to earthquake speeds, is controlled by shear stress drop in laboratory experiments[21,29,30] and in a one-dimensional (1D) continuous Burridge-Knopoff model[31], but the mechanical relationship between SSE and earthquake ruptures on elongated faults is not completely understood. Empirical moment-duration scaling relations[32–40] have been used to compare the physical mechanisms of SSEs and earthquakes, yet it is still debated whether the moment-duration scaling of SSEs is linear[32,33] or cubic[34–36] and a fundamental model that can unify SSEs and earthquakes is still missing. Here, I show that slow slip events are regular earthquakes with negligible dynamic-wave effects and the debated scaling behaviours of SSEs can be attributed to different length-scales of stress heterogeneities in faults.

General mechanism for steady SSEs and earthquakes

Previous theory[41] predicted that dip-slip ruptures on elongated faults in 3D elastic medium can steadily propagate at any speed up to the S-wave speed, if fracture energy increases with speed. Here, I test this hypothesis and realise such a continuum of rupture speeds (Figure S1A) in numerical simulations controlled by a rate-and-state friction law with rate-weakening behaviour at low slip rates and rate-strengthening behaviour at high slip rates, as observed in laboratory experiments[18–28] (Methods A1). The numerical simulations show that the steady rupture speed (v_r/v_s) is primarily controlled by two parameters (Figure 2a): the stress drop ($\Delta\tau/\sigma$) and the critical slip rate ($V_c\mu/\sigma v_s$) above which the fault friction transitions from rate-weakening to rate-strengthening. Here, the quantities are nondimensionalized by the S-wave speed (v_s), effective normal stress (σ), and shear modulus (μ)[42]. The rupture speed increases monotonically with the stress drop and critical slip rate. The change of rupture speed controlled by the stress drop is around one order of magnitude, while that controlled by the critical slip rate can be more than 6 orders of magnitude. Remarkably, these two parameters enable steady rupture propagation at a continuum of rupture speeds, including speeds of ultra-slow SSEs ($\ll v_s$), tsunami earthquakes[43–46] ($\sim \frac{1}{3}v_s$), and fast earthquakes ($> 0.5v_s$).

The dependence of rupture speed on stress drop is highly consistent for various values of critical slip rate except for the fast earthquakes (Figure S1b). The fast earthquakes deviate from the general trend of SSEs and tsunami earthquakes because of dynamic-wave effects. The effects of dynamic waves on rupture propagation have been theoretically investigated[41] and characterised by a nondimensional Lorentz contraction factor, $\alpha_s = \sqrt{1 - (v_r/v_s)^2}$, a well-known function in earthquake dynamics[47]. In addition, fracture mechanics theory shows that the analytical solutions of steady ruptures depend on $v_r/v_s/\alpha_s$ rather than v_r/v_s (Method A4). Therefore, the effects of dynamic waves are trivial when $v_r/v_s < 0.5$ (that is $v_r/v_s/\alpha_s \approx v_r/v_s$), a speed range including SSEs and tsunami earthquakes, and become significant as v_r approaches v_s (that is $v_r/v_s/\alpha_s \rightarrow \infty$). Accounting for the Lorentz factor, I find all values of rupture speeds of SSEs, tsunami and fast earthquakes, after normalization by the critical slip rate, collapse onto a universal curve (Figure 2b), which is predicted by the 3D theory of dynamic fracture mechanics of elongated ruptures (Methods A3 & A4). All values of peak slip rate also collapse onto the theoretical curve (Figure 2c). The collapses of the parameters and their consistency with the theory show that SSEs and earthquakes are mechanically the same and the link between them is the Lorentz contraction factor.

Steady rupture propagation with a continuum of speeds can be understood and quantitatively predicted by the 3D theory of dynamic fracture mechanics of elongated ruptures (Figure 1b). A basic condition for steady ruptures is the energy balance condition, $G_c = G_0$, where G_c is the dissipated fracture energy and G_0 is the energy release rate of subshear dip-slip ruptures[41]. In addition, a stability condition is necessary (Methods A5)

$$\frac{dG_c}{dV_p} > \frac{dG_0}{dV_p}, \tag{1}$$

where the peak slip rate V_p is interchangeable with the rupture speed v_r due to their monotonically increasing relation. Equation 1 requires that G_c increases with V_p faster than G_0, to suppress any tiny perturbation acting on the steady ruptures. The numerical simulations show that in all the simulated steady ruptures G_c agrees with G_0 within 3% (Figure S2a), which validates the energy balance condition. For steady ruptures, G_c increases with V_p (Figure S2b) while G_0 is a prescribed parameter independent of V_p (Methods A3), which validates the stability condition. The validations show that the two theoretical conditions are generic and their combination with a specific friction law leads to a practical rupture-tip equation-of-motion for steady ruptures on elongated faults.

Along-strike rupture segmentation

Further evidence of non-steady ruptures due to along-strike fault heterogeneities, such as piecewise-constant distributions of stresses, also demonstrate that SSEs and earthquakes are mechanically the same (Figure 3). When a steady rupture propagates into a segment of higher shear stress, the rupture jumps from one steady state to another via a transient (Figure 3a). The rupture speed transients of SSEs are very similar to those of tsunami earthquakes, while the transition distances of fast earthquakes are quantitatively longer due to the dynamic-wave effects. On the other hand, if the shear stress of the segment is lower than the minimum for steady ruptures, the segment behaves as a barrier, the rupture decelerates and finally arrests after penetrating a certain distance (Figure 3b). In general, the arresting distance increases with the peak slip rate before the rupture reaches the barrier, consistently between SSEs and tsunami earthquakes, while the arresting distances of fast earthquakes are longer due to the dynamic-wave effects. These non-steady ruptures show that the rupture behaviours of SSEs are the same as tsunami earthquakes and the quantitative differences between slow and fast earthquakes are caused by dynamic-wave effects.

The reason that fast earthquakes have longer transition and arresting distances than SSE and tsunami earthquakes can be understood by the 3D theory of dynamic fracture mechanics of elongated ruptures. Rupture propagation speed on elongated faults can be predicted by a theoretical rupture-tip equation-of-motion[41]: $F(G_c/G_0) = M(v_r/v_s)\ \dot{v}_r$, where F is an apparent force, M is an apparent mass, $\dot{v}_r$ is the rupture acceleration, the time derivative of rupture speed v_r, and G_c/G_0 is the energy ratio. The apparent mass $M(v_r/v_s)$ is nearly constant when $v_r/v_s < 0.5$ and increases to infinity as v_r approaches v_s (Methods A5), which is similar to the relativistic mass in Einstein's theory of relativity that contains the same Lorentz factor with the S-wave speed replaced by the speed of light. Because of this inertial effect, larger mass $M(v_r/v_s)$ due to high rupture speeds ($v_r \rightarrow v_s$) makes ruptures harder to stop within a barrier or to transition to another steady state, which therefore explains why the fast earthquakes require longer transition and arresting distances.

Geophysical observations[8,36,48,49] show that SSEs usually rupture each segment downdip of the seismogenic zone separately, but some SSEs can occasionally bridge multiple segments and reach larger magnitudes, which conceptually resembles the supercycle behaviour of large megathrusts earthquakes occurring in seismogenic zones[50,51]. This supercycle-like behaviour of SSEs can be explained by the time-dependent evolution of SSE segmentation. Both the theory and numerical simulations demonstrate that there is a critical stress drop for steady runaway SSEs (Figure 2b & Method A6), $\Delta\tau^{run} \approx 0.01\sigma$ where σ is the effective normal stress, above which the stability condition (equation 1) can be satisfied. On elongated dip-slip faults, a critical final slip is approximately related to the critical stress drop by $D^{run} = 2W\Delta\tau^{run}/\pi\mu$, where W is the SSE fault width and μ is the shear modulus[14]. SSE fault segments need to accumulate sufficient slip deficit (that is $> 0.02W\sigma/\pi\mu$) to be capable of accommodating runaway SSE ruptures, otherwise they act as barriers to stop rupture propagation. The recurrence interval of runaway SSE ruptures can be estimated by the ratio of D^{run} to the slip deficit rate on the fault segments during the inter-SSE period. The observed slip deficit rates on SSE fault segments in subduction zones globally are diverse, ranging from $< 10\%$ up to $> 50\%$ of the plate convergence rate[8,52–54], which can be explained by different values of fault properties in earthquake cycle simulations[55]. As rough lower bound estimates, values of $\sigma \sim 0.1 - 1$ MPa, $W \sim 40$ km, $\mu \sim 30$ GPa, and 100% of the plate convergence rate of 10^{-9} m/s yield $\Delta\tau^{run} \sim 0.001 - 0.01$ MPa and recurrence times of $\sim 0.4 - 4$ months, which are comparable to the typical stress drops, $0.001 - 0.2$ MPa[33,36,56], and typical recurrence times, months$-$years[8,57], of SSEs globally. Both theoretical and observational estimates of the recurrence times of SSEs are much shorter than those of large earthquakes, which are of the order of tens or hundreds of years[51]. Therefore, future investigations of the kinematics and dynamics of frequent SSEs shall enable the building of a comprehensive supercycle model, which in turn will help to better understand the supercycle behaviour of the large devastating earthquakes.

Observations of SSEs and earthquakes

The comparison of moment-duration scaling relations between SSEs and earthquakes has been considered in discussions of their physical mechanisms[32–40], however the moment-duration relation of SSEs observed in a particular environment features a cubic scaling[34–36] that is radically different from the linear scaling observed in a global compilation[32,33]. Here, I show that the different scaling behaviours can be attributed to different length-scales of stress heterogeneities: heterogeneity of shear stress within a fault can produce a cubic scaling, whereas heterogeneity of effective normal stress among different fault environments produces a linear scaling. For elongated ruptures, the relation[58] between moment (M_0) and duration (T) is $M_0 \propto \Delta\tau W^2 L$, where $L = v_r T$ is the rupture length and $\Delta\tau$ and v_r are the stress drop and rupture speed, respectively. Defining $\Delta\tau \propto L^\alpha$ and $v_r \propto L^\beta$ leads to $M_0 \propto T^{\frac{1+\alpha}{1-\beta}}$, where α and β are constant coefficients. For a homogeneous model (Methods A7), ruptures with different values of $\Delta\tau$ produce a linear moment-duration scaling (Figure 4a). However if the shear stress distribution in the fault is heterogeneous, and in particular if it decays linearly away from the nucleation area (Methods A7), the simulated models result in $\alpha = 0.5$ and $\beta = 0.5$, which leads to a cubic scaling relation (Figure 4a & S3). Although this is one specific case of heterogeneity, it demonstrates that a cubic scaling relation can be produced by heterogeneity of shear stress within a particular fault, as also observed in an SSE cycle model[40]. Moreover, such cubic scaling curve, assuming constant effective normal stress σ, can be diagonally shifted in the $M_0 - T$ space if σ systematically varies (Figure 4b), as predicted by the theoretical relations $M_0 \propto \sigma$ and $T \propto \sigma$ (Method A7). A linear envelope scaling can be obtained by mixing data with diverse values of σ in different fault environments, which can explain the observed linear scaling based on a global compilation of slow earthquakes[32,33]. In addition, another theoretical relation, $T \propto 1/V_c$ (Methods A7), predicts that as the critical slip rate increases the cubic scaling of SSEs can be shifted vertically toward that of earthquakes, which can reconcile the separation between the cubic scaling of SSEs and earthquakes.

To explore a universal scaling relation in the global dataset that is consistent with fracture mechanics theory, I calculate the rupture speed and peak slip rate of the SSEs and tsunami earthquakes observed globally[36,44–46,59]. The rupture speed is estimated by $v_r = L/T$, with an uncertainty of a factor of 2 for bilateral ruptures. The peak slip rate is estimated by $V_p = \gamma D/\tau_{rise}$, where D is the slip, τ_{rise} is the rise time, and $\gamma \approx 20$ is an empirical ratio between the peak and average slip rates in numerical simulations (Figure S4). For pulse ruptures on elongated faults, the rise time is approximately estimated by $\tau_{rise} = TW/L$. In general, there is an increasing trend between the observed rupture speed and peak slip rate, enveloped by two theoretical predictions assuming constant strength drops of $5\ MPa$ and $0.05\ MPa$ (Figure 4c). Least squares regression between the nondimensionalized quantities of the global observations and the theoretical prediction constrains the best values of the critical slip rate and effective normal stress (Figure 4d): $V_c = 2 \times 10^{-9}$ m/s and $\sigma = 0.2$ MPa for the Cascadia subduction zone, $V_c = 10^{-9}$ m/s and $\sigma = 0.4$ MPa for the Japan subduction zone, and $V_c = 10^{-3}$ m/s and $\sigma = 10$ MPa for tsunami earthquakes worldwide.

A continuum of rupture speeds from SSE speeds up to the S-wave speed has been reported in laboratory experiments for a wide range of stress drop[29]. The basic model developed here predicts that such a continuum of speeds shall prevail in natural environments if wide ranges of $V_c\mu/\sigma v_s$ and $\Delta\tau/\sigma$ are available (Figure 2a). A wide range of V_c between $10^{-9}\ m/s$ and $10^{-2}\ m/s$ has been reported in laboratory friction experiments on both natural and synthetic fault gouges[22–28]. Other frictional mechanisms, such as fault gouge dilatancy with associated change in fluid pressure[60–63], could also play a role in the frictional transition, but the values of $V_c\mu/\sigma v_s$ remain to be determined. If the values of V_c in the natural environments are as diverse as the laboratory observations, then continuous rupture speeds of SSEs are expected, otherwise, the current model predicts a rupture speed gap that depends on the unavailable range of $V_c\mu/\sigma v_s$. So far, no large SSE ($M_w > 6$) of

$v_r > 1\ m/s$ has been detected (Figure 4c), although such SSEs would be detectable by continuous GPS. But, recent studies have made progress in detecting smaller SSEs by connecting seismic and geodetic data[35,64] or by examining the spatiotemporal features of tremors[65] and low-frequency earthquakes[66], whose rupture speeds might lie within the speed gap. More work is needed in the future that can either fill the observational gap of rupture speeds shown in Figure 4c, or explain why V_c in nature is not as diverse as in the laboratory observations.

Earthquake ruptures on elongated faults can steadily propagate at speeds of $\sim \frac{1}{3}v_s$ if $V_c\mu/\sigma v_s > 10^{-4}$, which provides a new mechanism to explain the anomalously slow tsunami earthquakes[43–46]. Given $\sigma = 10\ MPa$, values of V_c are required to be larger than $10^{-4}\ m/s$, which is supported by laboratory experiments[22,25–27], although the frictional strength may change from rate-strengthening to rate-weakening at slip rates higher than $0.1\ m/s$ due to the strong weakening mechanisms that facilitate the fast earthquakes[25–27,67]. The narrow range of rate-strengthening behaviour between $\sim 10^{-4}\ m/s$ and $0.1\ m/s$ may explain the scarcity of tsunami earthquakes. The alternative explanations for tsunami earthquakes are low rigidity materials[68,69] and inelastic material within and/or around the fault[70], and the density and size of asperities[71], which remain to be confirmed by further investigations.

Although the current theoretical model and previous studies[35,38,65] have suggested a continuous spectrum of slip mode, further investigations are warranted to monitor and constrain rupture kinematics and dynamics of global SSEs over a wider spectrum of rupture speeds. The supercycle model of large earthquakes[50,51], which would enable assessment of the future seismic hazard, has not yet been validated by at least one complete cycle of modern seismological data, due to their long recurrence intervals. The rupture behaviours of SSEs, whose recurrence intervals are much shorter than the large earthquakes, have been unified with regular earthquakes by the basic theory of rupture dynamics, and therefore can be used to understand the supercycle behaviour of large devastating earthquakes.

Methods

A1. Quasi-dynamic SSE rupture simulations I consider a 3D dip-slip rupture problem on an infinitely long fault with finite seismogenic width W embedded in a full-space, linear elastic, homogeneous medium. This 3D elongated rupture problem has been successfully approximated by a reduced-dimensionality (2.5D) model, which accounts for the elongated features while having a low computational cost[15,41]. To facilitate a comprehensive comparison between numerical simulations and fracture mechanics theory, I investigate the rupture propagation of SSEs and earthquakes using 2.5D single-rupture simulations with prescribed initial conditions. The simulations of SSEs are quasi-dynamic, while the simulations of earthquakes are fully dynamic, as explained in Methods A2. The shear modulus and S-wave speed of the medium are denoted μ and v_s, respectively.

The frictional strength, τ, of faults is controlled by a rate-and-state friction law with rate-weakening behaviour at low slip rates and rate-strengthening behaviour at high slip rates[72], which has been used to investigate the rupture propagation of SSEs[15–17,73]

$$\tau = f^* \sigma + a\sigma \ln\left(\frac{V}{V^*}\right) + b\sigma \ln\left(\frac{V_c \theta}{D_c} + 1\right), \tag{2}$$

where σ is the effective normal stress, f^* and V^* are arbitrary reference values, D_c is the characteristic slip distance, a and b are nondimensional parameters, V is the slip rate, θ is the state, and V_c is a critical slip rate. Rock exhibits rate-weakening frictional behaviour when $a - b < 0$, and the critical slip rate V_c controls the transition from rate-weakening to rate-strengthening[15]. The evolution of state θ is described by the aging law[74]

$$\dot{\theta} = 1 - \frac{V\theta}{D_c}, \tag{3}$$

where $\dot{\theta}$ is the time derivative of θ.

For each single-rupture model, one of the primary parameters that affects the rupture propagation is the initial shear stress τ_i, which equals to the frictional strength and is prescribed by the values of initial slip rate V_i and state θ_i

$$\tau_i = f^*\sigma + a\sigma \ln\left(\frac{V_i}{V^*}\right) + b\sigma \ln\left(\frac{V_c\theta_i}{D_c} + 1\right), \tag{4}$$

The nondimensional parameters, a/b and W/L_b, also affect the rupture propagation[15], where

$$L_b = \frac{\mu D_c}{b\sigma}. \tag{5}$$

In this study, I fix the nondimensional ratios of $a/b = 0.8$ and $W/L_b = 400$, and systematically vary τ_i and V_c. The specific values of the frictional parameters are prescribed as: $\sigma = 20\ MPa$, $b = 0.015$, $W = 40\ km$, $D_c = 10^{-3}\ m$, $f^* = 0.6$, and $V^* = 10^{-9}\ m/s$; although the choice of them doesn't affect the conclusion of this paper because both the computational and analytical results are presented in nondimensional form. To facilitate the comparison with fracture mechanics theory, the loading due to the plate convergence during rupture propagation is not considered and the systematically varied τ_i in this study represents different interseismic or inter-SSE phases.

A nucleation zone of length $0.5W$ with higher slip rates ($\geq 10V_c$) is prescribed to smoothly nucleate unilateral ruptures. Outside the nucleation zone rupture propagation is spontaneous. A stronger nucleation, such as the overstressed nucleation condition, results in slight oscillations of rupture speed in the fully dynamic rupture models, but does not affect the steady rupture speed (Figure S5). I use the boundary element software QDYN[75] for the quasi-dynamic SSE simulation, where the fault is infinitely long and the fault slip is horizontally periodic with a prescribed length, $11W$. To avoid the interaction of the periodic fault segments, a buffing segment of length $5.5W$ is set, where the frictional behaviour is rate-strengthening with $a > b$. Sufficient numerical resolution is guaranteed by setting a small grid size (Δx), that is, $L_c/\Delta x = 8$. The simulated time is set long enough to capture the whole rupture propagation. For each single-rupture model, the rupture time on each node of faults is determined by a criterion of slip rate, $10V_i$, and the rupture speed is computed based on the along-strike gradient of the rupture time.

A2. Fully dynamic earthquake rupture simulations The 2.5D single-rupture simulations for earthquakes are fully dynamic, conducted by a spectral element software SEM2DPACK[76]. For a quantitative comparison between SSE and earthquake simulations, the same friction law and parameters are assumed in the dynamic earthquake rupture simulations, except for larger values of V_c, and the additional thermal weakening[67,77] at slip rate $> 0.1\ m/s$ is not considered. Previous theoretical studies[41] have suggested that the additional thermal weakening can affect the rupture speeds via controlling the dissipated[78] and potential[77] energies on faults, which remains to be quantitatively investigated in the future. For simulations with rupture speeds close to the S-wave speed, a sufficiently large computational domain is set to avoid the effects of the reflected waves from the domain boundaries within the simulated time. For simulations with slow rupture speeds, the seismic radiation is relatively weak and can be well absorbed by the default absorbing boundaries in SEM2DPACK, and therefore, the simulated times are allowed to be several times longer than those for fast rupture speeds. The time step is set based on the Courant-Friedrichs-Lewy stability condition, and the grid size is the same as the quasi-dynamic SSE simulation, that is $L_c/\Delta x = 8$.

A3. Energy balance of steady SSEs and earthquakes For SSE and earthquake ruptures on long faults with finite width W, the energy release rate and dissipated fracture energy can be derived in the theoretical framework of 3D dynamic fracture mechanics of elongated ruptures. The energy release rate G_0 is the rate of mechanical energy flow into the rupture tip per unit rupture advance, which is dissipated by the fracture energy G_c for steady ruptures. For dip-slip faulting, the energy release rate G_0 depends on the static stress drop ($\Delta\tau$) and fault width:

$$G_0 = \frac{\lambda \Delta\tau^2 W}{\mu}, \tag{6}$$

where λ is a geometrical factor, with $\lambda = 1/\pi$ for a deep buried fault[41]. The fracture energy G_c depends on the strength evolution on the fault[79]:

$$G_c = \int_0^D [\tau(\delta) - \tau(D)] \cdot d\delta, \tag{7}$$

where $\tau(\delta)$ is the fault strength as a function of fault slip δ and D is the final slip. Equations 6 and 7 are the generic definitions of energies of ruptures on elongated faults regardless of the specific friction law. Below, I propose an approach to estimate G_0 and G_c under the framework of the V-shape rate-and-state friction law explained in Methods A1.

G_0 is a function of the static stress drop, the difference of shear stress before and after the ruptures

$$\Delta\tau = \tau_i - \tau_f, \tag{8}$$

where τ_i are τ_f are the initial shear stress and final shear stress, respectively. Previous rupture simulations of V-shape rate-and-state friction[15] have shown that the fault strength approximately drops to the minimum steady-state strength and stays there until the end of the ruptures, which is a feature different from the regular rate-and-state friction law with aging law[80]. The minimum steady-state strength[15] is

$$\tau_f = f^*\sigma + a\sigma \ln\left(\frac{b-a}{a}\frac{V_c}{V^*}\right) + b\sigma \ln\left(\frac{a}{b-a} + 1\right). \tag{9}$$

Combining equations 4 and 8 yields the close-form static stress drop

$$\Delta\tau = a\sigma \ln \frac{aV_i}{(b-a)V_c} + b\sigma \ln \frac{\frac{V_c\theta_i}{D_c} + 1}{\frac{a}{b-a} + 1}. \tag{10}$$

Equation 10 well predicts the numerical values of $\Delta\tau$ in all the simulated steady models (Figure S2c). Substituting equation 10 into equation 6 yields the theoretical energy release rate

$$G_0 = \frac{\lambda b^2\sigma^2 W}{\mu} \cdot \left[\frac{a}{b} \ln \frac{aV_i}{(b-a)V_c} + \ln \frac{\frac{V_c\theta_i}{D_c} + 1}{\frac{a}{b-a} + 1}\right]^2. \tag{11}$$

The main feature in equation 11 is that G_0 only depends on the prescribed parameters and is independent of the peak slip rate V_p. As only τ_i and V_c are systematically investigated in this study, G_0 can be written as $G_0(\tau_i, V_c)$.

G_c is an integral function of the fault strength $\tau(\delta)$ about the slip δ. The numerical simulations show that fault strength governed by V-shape rate-and-state friction has two weakening stages: the first stage accounts for the fast weakening process within the narrow cohesive zone and the second stage accounts for the slow weakening process outside the cohesive zone (Figure S6). In the first weakening stage, the strength drop $\Delta\tau_{p-r}$ and the critical slip-weakening distance d_c

can be well predicted by previous theoretical equations[15]

$$\begin{aligned}\Delta\tau_{p-r} &= b\sigma\Big[\ln\big(\frac{V_c\theta_i}{3D_c}+1\big)-\ln\big(\frac{3V_c}{V_p}+1\big)\Big],\\ d_c &= D_c\Big[\ln\big(\frac{V_c\theta_i}{3D_c}+1\big)-\ln\big(\frac{3V_c}{V_p}+1\big)\Big],\end{aligned}\tag{12}$$

where V_p is the peak slip rate and the factor 3 is an approximation of the non-uniform slip rate within the cohesive zone, which was proposed to be 2 by Hawthorne and Rubin[15]. Thus, the fracture energy within the cohesive zone is estimated as

$$G_{c1}=\frac{1}{2}d_c\Delta\tau_{p-r}=\frac{1}{2}b\sigma D_c\Big[\ln\big(\frac{V_c\theta_i}{3D_c}+1\big)-\ln\big(\frac{3V_c}{V_p}+1\big)\Big]^2.\tag{13}$$

The contribution of fracture energy of the second weakening stage has not explicitly been considered before. Here, I account for this part of the total fracture energy by

$$G_{c2}=\frac{1}{2}(d_c+D)(\tau_r-\tau_f),\tag{14}$$

where D is the final slip, $\tau_r-\tau_f$ is the overshooting stress, and τ_r is the fault strength at the tail of the cohesive zone

$$\tau_r=f^*\sigma+a\sigma\ln\left(\frac{V_p}{3V^*}\right)+b\sigma\ln\left(\frac{3V_c}{V_p}+1\right),\tag{15}$$

$$\tau_r-\tau_f=a\sigma\ln\left(\frac{aV_p}{3(b-a)V_c}\right)+b\sigma\ln\left(\frac{\frac{3V_c}{V_p}+1}{\frac{a}{b-a}+1}\right).\tag{16}$$

For ruptures on long faults with finite width W, the final slip D is linearly proportional to the static stress drop $\Delta\tau$, that is[14]

$$D=\frac{2\lambda W}{\mu}\cdot\Delta\tau.\tag{17}$$

Substituting equations 10, 17, 12, and 16 into equation 14 yields the close-form function of the second part of the fracture energy, G_{c2}. Therefore, the close-form function of total fracture energy is given by $G_c = G_{c1} + G_{c2}$. As G_c depends on τ_i, V_c, and the undetermined peak slip rate V_p, it can be written as $G_c(V_p, \tau_i, V_c)$.

For steady ruptures, the energy release rate shall be balanced by the dissipated fracture energy:

$$G_c(V_p, \tau_i, V_c) = G_0(\tau_i, V_c). \tag{18}$$

Equation 18 shows that the peak slip rate V_p of steady ruptures can be uniquely determined from the energy balance condition of V-shape rate-and-state friction. I find that equation 18 well predicts the relations among V_p, $\Delta\tau$, G_0, and G_c in all the simulated steady ruptures (Figure 2c & S2).

A4. Relation between peak slip rate and rupture speed A linear relation between peak slip rate and rupture speed for steady SSEs has been proposed by Hawthorne and Rubin[15]

$$V_p = \frac{v_r}{C} \cdot \frac{\Delta\tau_{p-r}}{\mu}, \tag{19}$$

where $C \approx 0.5 - 0.55$ is an empirical geometrical factor. But this relation does not include the effects of dynamic waves when the rupture speed approaches the S-wave speed. Alternatively, Gabriel et al[81] have provided a theoretical relation between peak slip rate and rupture speed for 2D strike-slip faulting earthquakes whose rupture speeds are close to the S-wave speed. Here, I extend their 2D strike-slip relation to a dip-slip relation for 3D elongated rupture problem, which physically incorporates equation 19, as explained below.

Weng and Ampuero[41] demonstrated that if the cohesive zone size on elongated faults is much smaller than fault width, $L_c \ll W$, then the energy release rate has the following form:

$$G_{tip} = \frac{1}{2\mu} A(v_r) K_{tip}^2, \tag{20}$$

where $A(v_r) = 1/\alpha_s$, $\alpha_s = \sqrt{1 - (v_r/v_s)^2}$ is the Lorentz contraction term and K_{tip} is the stress intensity factor. By removing the strike-slip term $1 - \nu$ and replacing $A(v_r)$ by $1/\alpha_s$ in equation (18) in Gabriel et al[81], I obtain the dip-slip relation between peak slip rate and rupture speed, similar to a classical 2D result[82]

$$V_p = \frac{v_r}{\alpha_s} \cdot \frac{2\Delta\tau_{p-r}}{\mu}, \tag{21}$$

where the correction of a factor of 2 is made to fit the numerical results. If $v_r \ll v_s$, then the Lorentz term $\alpha_s = 1$, and equation 21 is the same as equation 19 proposed for SSEs by Hawthorne and Rubin[15]. Note that $\Delta\tau_{p-r}$ is a function of V_p/V_c (equation 12), and thus equation 21 can be written as

$$\frac{v_r/V_c}{\alpha_s} = \frac{\mu}{2} \cdot \frac{V_p/V_c}{\Delta\tau_{p-r}}. \tag{22}$$

Equation 22 and 18 can well predict the relation among stress drop, peak slip rate, and rupture speed for both SSEs and earthquakes (Figure 2).

A5. Stability conditions for steady ruptures on elongated faults Rupture propagation on elongated faults can be predicted by a theoretical rupture-tip equation-of-motion[41]

$$F(G_c/G_0) = M(v_r) \cdot \dot{v}_r, \tag{23}$$

where

$$\begin{aligned} F(G_c/G_0) &= 1 - G_c/G_0, \\ M(v_r) &= \frac{W}{v_s^2} \frac{\gamma}{A\alpha_s^P}, \end{aligned} \tag{24}$$

G_c and G_0 are the fracture energy and energy release rate, γ, A, and P are known coefficients, and $\alpha_s = \sqrt{1-(v_r/v_s)^2}$ is the Lorentz contraction factor. $M(v_r)$ is nearly constant when $v_r/v_s \ll 1$ and increases to infinity when $v_r/v_s \to 1$. For a steady rupture, the acceleration $\dot{v}_r$ is zero, thus $G_c = G_0$, which is the energy balance condition. In addition, the stability of steady ruptures also depends on the sign of $dF(G_c/G_0)/dv_r$. If $dF(G_c/G_0)/dv_r > 0$, a tiny positive/negative perturbation of v_r acting on the steady rupture induces a further increase/decrease of v_r. Therefore, $dF(G_c/G_0)/dv_r < 0$ is another condition for steady ruptures. Combining this inequality equation with $G_c = G_0$ results in

$$\frac{dG_c}{dv_r} > \frac{dG_0}{dv_r}. \tag{25}$$

Considering the monotonic relation between v_r and V_p (Method A4), equation 25 can also be written as

$$\frac{dG_c}{dV_p} > \frac{dG_0}{dV_p}. \tag{26}$$

Therefore, $G_c = G_0$ and equation 25 are two generic conditions for steady ruptures on elongated faults independent of the specific friction law.

A6. Critical stress drop for runaway ruptures I approximately derive the minimum stress drop for runaway/steady ruptures. Under the framework of V-shape rate-and-state friction law, G_0 and G_c can be written as

$$\begin{aligned} G_0 &= \frac{\lambda W}{\mu}\Delta\tau^2, \\ G_c &= \frac{\lambda W}{\mu}\left[\frac{L_c}{2\lambda W}\Delta\tau_{p-r}^2 + \big(\frac{L_c}{2\lambda W}\Delta\tau_{p-r} + \Delta\tau\big)(\tau_r - \tau_f)\right]. \end{aligned} \tag{27}$$

For runaway/steady ruptures, the energy balance condition of equation 27 is

$$\left(\frac{\Delta\tau}{b\sigma}\right)^2 = \frac{L_c}{2\lambda W}\left(\frac{\Delta\tau_{p-r}}{b\sigma}\right)^2 + \left(\frac{L_c}{2\lambda W}\frac{\Delta\tau_{p-r}}{b\sigma} + \frac{\Delta\tau}{b\sigma}\right)\frac{\tau_r - \tau_f}{b\sigma}. \tag{28}$$

Assuming the fault is steady-state before rupture, that is $V_i\theta_i/D_c = 1$, equations 10 and 12 yield a lengthy expression of $\Delta\tau_{p-r}/b\sigma$ that depends on $\Delta\tau/b\sigma$, a/b, and V_p/V_c. Although the derivation of closed-form $\Delta\tau$ is complex and lengthy, the dimensional analysis of equation 28 shows that $\Delta\tau/b\sigma$ is a function of V_p/V_c, a/b, and W/L_c. For an extreme condition, $W/L_c \gg 1$, equations 28 and 16 leads to a minimum stress drop

$$\frac{\Delta\tau^{run}}{b\sigma} = \frac{a}{b}\ln\left(\frac{aV_p}{3(b-a)V_c}\right) + \ln\left(\frac{\frac{3V_c}{V_p}+1}{\frac{a}{b-a}+1}\right). \tag{29}$$

Hawthorne and Rubin[15] noted that the minimum stress drop for steady ruptures can be approximated with $V_p/V_c \approx 15(b-a)/a$. Here, I approximately use the value of $V_p/V_c \approx 30(b-a)/a$ and numerically solve $\Delta\tau/b\sigma$ in equations 28 and 29, which can explain the current single-rupture simulation results with an uncertainty of a factor of 2 (Figure S7). Given the values of $a/b = 0.8$, $b = 0.015$, and $W/L_c = 400$ used in this paper, the critical stress drop for runaway ruptures is about $\Delta\tau^{run} \approx 0.01\sigma$. Substituting the critical stress drop and minimum peak slip rate into equations 22 yields $v_r^{run} \approx 50\alpha_s V_c\mu/\sigma$.

A7. Moment-duration scaling relations of SSEs I simulate single-rupture models by prescribing different values of initial shear stress to obtain moment-duration scaling relations of SSEs. The other model parameters are fixed and are the same as those described in Methods A1, except for a smaller $W/L_b = 100$ that reduces the computational cost and thus allows for a longer simulated fault, $20W$. For the homogeneous shear stress model, the stress drop is always lower than the runaway stress drop $\Delta\tau^{run}$, which only results in self-arresting ruptures. For the linearly decaying shear stress model, the initial shear stress is largest near the nucleation zone and linearly decreases to zero at the other side of the fault. A minimum nucleation length, $0.1W$, with higher slip rates is prescribed to smoothly nucleate unilateral ruptures. For each rupture model, the rupture length, L, is determined by the end of the rupture tip, and the SSE duration, T, is estimated by a slip rate threshold, $0.1V_c$. Note that the SSE duration is slightly longer than the rupture time by a rise time. As the prescribed initial shear stress increases, the rupture length L, moment M_0, and duration T of SSEs increase accordingly. In the homogeneous shear stress model, L and M_0 increase toward infinity as stress drop asymptotically approaches $\Delta\tau^{run}$.

For elongated ruptures, the moment is $M_0 \sim \Delta\tau W^2 L$, where L is the rupture length and $\Delta\tau$ and v_r are the average stress drop and rupture speed, respectively. The duration is $T \approx L/v_r$. The theory and numerical simulations predict two characteristic quantities for runaway SSEs (Figure 2b): $\Delta\tau^{run} \approx 0.01\sigma$ and $v_r^{run} \approx 50V_c\mu/\sigma$, where σ is the effective normal stress, V_c is the critical slip rate, and μ is the shear modulus. Therefore, the moment and duration can be normalized

$$\begin{aligned} \frac{M_0}{\Delta\tau^{run}W^3} &\sim \frac{\Delta\tau}{\Delta\tau^{run}} \cdot \frac{L}{W} \\ \frac{T}{W/v_r^{run}} &\sim \frac{v_r^{run}}{v_r} \cdot \frac{L}{W}. \end{aligned} \tag{30}$$

In the numerical simulations, L/W, $\Delta\tau/\Delta\tau^{run}$, and v_r/v_r^{run} are calculated. Defining $\Delta\tau/\Delta\tau^{run} \propto (L/W)^\alpha$ and $v_r/v_r^{run} \propto (L/W)^\beta$ leads to

$$\frac{M_0}{\Delta\tau^{run}W^3} \sim \left(\frac{T}{W/v_r^{run}}\right)^{\frac{1+\alpha}{1-\beta}} \tag{31}$$

In the homogeneous shear stress model, if $\Delta\tau > \Delta\tau^{run}$, runaway ruptures steadily propagate through the entire fault with $\Delta\tau$ and v_r independent of rupture length L, that is $\alpha = 0$ and $\beta = 0$. If $\Delta\tau < \Delta\tau^{run}$, self-arresting ruptures decelerate and gradually stop for various values of $\Delta\tau$, which roughly results in $\alpha = 0.25$ and $\beta = -0.25$ (Figure S3). Therefore, both runaway and self-arresting ruptures in the homogeneous stress model produce a linear moment-duration scaling relation. In the linearly decaying shear stress model, the simulated models result in $\alpha = 0.5$ and $\beta = 0.5$ (Figure S3), which leads to a cubic scaling relation.

Because $\Delta\tau \propto \sigma$ and $v_r \propto 1/\sigma$ (equations 10, 22, and 12), the dimensional analysis of equation 30 shows that α and β are independent of σ, $M_0 \propto \Delta\tau^{run} \propto \sigma$, and $T \propto \frac{1}{v_r^{run}} \propto \sigma$. Therefore, as σ systematically varies, the scaling curve between $M_0/(\Delta\tau^{run}W^3)$ and $T/(W/v_r^{run})$ is invariable (Figure 4a), while the scaling curve between M_0 and T moves diagonally in the $M_0{-}T$ space (Figure 4b). In addition, similar dimensional analysis shows that M_0 is independent of V_c and $T \sim 1/V_c$. As V_c systematically varies, the scaling curve between M_0 and T moves vertically in the $M_0 - T$ space.

1. Hirose, H., Hirahara, K., Kimata, F., Fujii, N. & Miyazaki, S. A slow thrust slip event following the two 1996 hyuganada earthquakes beneath the bungo channel, southwest japan. *Geophysical Research Letters* **26**, 3237–3240 (1999).

2. Dragert, H., Wang, K. & James, T. S. A silent slip event on the deeper cascadia subduction interface. *Science* **292**, 1525–1528 (2001).

3. Lowry, A. R., Larson, K. M., Kostoglodov, V. & Bilham, R. Transient fault slip in guerrero, southern mexico. *Geophysical Research Letters* **28**, 3753–3756 (2001).

4. Ozawa, S., Murakami, M. & Tada, T. Time-dependent inversion study of the slow thrust event in the nankai trough subduction zone, southwestern japan. *Journal of Geophysical Research: Solid Earth* **106**, 787–802 (2001).

5. Ohta, Y., Freymueller, J. T., Hreinsdóttir, S. & Suito, H. A large slow slip event and the depth of the seismogenic zone in the south central alaska subduction zone. *Earth and Planetary Science Letters* **247**, 108–116 (2006).

6. Douglas, A., Beavan, J., Wallace, L. & Townend, J. Slow slip on the northern hikurangi subduction interface, new zealand. *Geophysical Research Letters* **32** (2005).

7. Outerbridge, K. C. *et al.* A tremor and slip event on the cocos-caribbean subduction zone as measured by a global positioning system (gps) and seismic network on the nicoya peninsula, costa rica. *Journal of Geophysical Research: Solid Earth* **115** (2010).

8. Michel, S., Gualandi, A. & Avouac, J.-P. Interseismic coupling and slow slip events on the cascadia megathrust. *Pure and Applied Geophysics* **176**, 3867–3891 (2019).

9. Rousset, B., Bürgmann, R. & Campillo, M. Slow slip events in the roots of the san andreas fault. *Science advances* **5**, eaav3274 (2019).

10. Kato, A. *et al.* Propagation of slow slip leading up to the 2011 mw 9.0 tohoku-oki earthquake. *Science* **335**, 705–708 (2012).

11. Ruiz, S. *et al.* Intense foreshocks and a slow slip event preceded the 2014 iquique mw 8.1 earthquake. *Science* **345**, 1165–1169 (2014).

12. Rousset, B. *et al.* An aseismic slip transient on the north anatolian fault. *Geophysical Research Letters* **43**, 3254–3262 (2016).

13. Uchida, N., Iinuma, T., Nadeau, R. M., Bürgmann, R. & Hino, R. Periodic slow slip triggers megathrust zone earthquakes in northeastern japan. *Science* **351**, 488–492 (2016).

14. Weng, H. & Ampuero, J.-P. Continuum of earthquake rupture speeds enabled by oblique slip. *Nature Geoscience* 1–5 (2020).

15. Hawthorne, J. & Rubin, A. Laterally propagating slow slip events in a rate and state friction model with a velocity-weakening to velocity-strengthening transition. *Journal of Geophysical Research: Solid Earth* **118**, 3785–3808 (2013).

16. Shibazaki, B. & Iio, Y. On the physical mechanism of silent slip events along the deeper part of the seismogenic zone. *Geophysical Research Letters* **30** (2003).

17. Shibazaki, B. & Shimamoto, T. Modelling of short-interval silent slip events in deeper subduction interfaces considering the frictional properties at the unstable—stable transition regime. *Geophysical Journal International* **171**, 191–205 (2007).

18. Im, K., Saffer, D., Marone, C. & Avouac, J.-P. Slip-rate-dependent friction as a universal mechanism for slow slip events. *Nature Geoscience* **13**, 705–710 (2020).

19. Ikari, M. J., Marone, C., Saffer, D. M. & Kopf, A. J. Slip weakening as a mechanism for slow earthquakes. *Nature geoscience* **6**, 468–472 (2013).

20. Kaproth, B. M. & Marone, C. Slow earthquakes, preseismic velocity changes, and the origin of slow frictional stick-slip. *Science* **341**, 1229–1232 (2013).

21. Leeman, J., Saffer, D., Scuderi, M. & Marone, C. Laboratory observations of slow earthquakes and the spectrum of tectonic fault slip modes. *Nature communications* **7**, 1–6 (2016).

22. Weeks, J. D. Constitutive laws for high-velocity frictional sliding and their influence on stress drop during unstable slip. *Journal of Geophysical Research: Solid Earth* **98**, 17637–17648 (1993).

23. Shimamoto, T. Transition between frictional slip and ductile flow for halite shear zones at room temperature. *Science* **231**, 711–714 (1986).

24. Kilgore, B. D., Blanpied, M. L. & Dieterich, J. H. Velocity dependent friction of granite over a wide range of conditions. *Geophysical Research Letters* **20**, 903–906 (1993).

25. Reches, Z. & Lockner, D. A. Fault weakening and earthquake instability by powder lubrication. *Nature* **467**, 452–455 (2010).

26. Liao, Z., Chang, J. C. & Reches, Z. Fault strength evolution during high velocity friction experiments with slip-pulse and constant-velocity loading. *Earth and Planetary Science Letters* **406**, 93–101 (2014).

27. Buijze, L., Niemeijer, A. R., Han, R., Shimamoto, T. & Spiers, C. J. Friction properties and deformation mechanisms of halite (-mica) gouges from low to high sliding velocities. *Earth and Planetary Science Letters* **458**, 107–119 (2017).

28. Rabinowitz, H. *et al.* Frictional behavior of input sediments to the hikurangi trench, new zealand. *Geochemistry, Geophysics, Geosystems* **19**, 2973–2990 (2018).

29. Passelègue, F. X. *et al.* Initial effective stress controls the nature of earthquakes. *Nature communications* **11**, 1–8 (2020).

30. Scuderi, M. M., Collettini, C., Viti, C., Tinti, E. & Marone, C. Evolution of shear fabric in granular fault gouge from stable sliding to stick slip and implications for fault slip mode. *Geology* G39033.1 (2017).

31. Bar Sinai, Y., Brener, E. A. & Bouchbinder, E. Slow rupture of frictional interfaces. *Geophysical Research Letters* **39** (2012).

32. Ide, S., Beroza, G. C., Shelly, D. R. & Uchide, T. A scaling law for slow earthquakes. *Nature* **447**, 76–79 (2007).

33. Gao, H., Schmidt, D. A. & Weldon, R. J. Scaling relationships of source parameters for slow slip events. *Bulletin of the Seismological Society of America* **102**, 352–360 (2012).

34. Gomberg, J., Wech, A., Creager, K., Obara, K. & Agnew, D. Reconsidering earthquake scaling. *Geophysical Research Letters* **43**, 6243–6251 (2016).

35. Frank, W. B. & Brodsky, E. E. Daily measurement of slow slip from low-frequency earthquakes is consistent with ordinary earthquake scaling. *Science advances* **5**, eaaw9386 (2019).

36. Michel, S., Gualandi, A. & Avouac, J.-P. Similar scaling laws for earthquakes and cascadia slow-slip events. *Nature* **574**, 522–526 (2019).

37. Takagi, R., Uchida, N. & Obara, K. Along-strike variation and migration of long-term slow slip events in the western nankai subduction zone, japan. *Journal of Geophysical Research: Solid Earth* **124**, 3853–3880 (2019).

38. Peng, Z. & Gomberg, J. An integrated perspective of the continuum between earthquakes and slow-slip phenomena. *Nature geoscience* **3**, 599–607 (2010).

39. Thøgersen, K., Andersen Sveinsson, H., Scheibert, J., Renard, F. & Malthe-Sørenssen, A. The moment duration scaling relation for slow rupture arises from transient rupture speeds. *Geophysical Research Letters* **46**, 12805–12814 (2019).

40. Dal Zilio, L., Lapusta, N. & Avouac, J. Unraveling scaling properties of slow-slip events. *Geophysical Research Letters* **47**, e2020GL087477 (2020).

41. Weng, H. & Ampuero, J. The dynamics of elongated earthquake ruptures. *Journal of Geophysical Research: Solid Earth* (2019).

42. Barenblatt, G. I., Barenblatt, G. I. & Isaakovich, B. G. *Scaling, self-similarity, and intermediate asymptotics: dimensional analysis and intermediate asymptotics* (Cambridge University Press, 1996).

43. Kanamori, H. Mechanism of tsunami earthquakes. *Physics of the earth and planetary interiors* **6**, 346–359 (1972).

44. Kikuchi, M. & Kanamori, H. *Source characteristics of the 1992 Nicaragua tsunami earthquake inferred from teleseismic body waves*, 441–453 (Springer, 1995).

45. Ihmlé, P. F., Gomez, J.-M., Heinrich, P. & Guibourg, S. The 1996 peru tsunamigenic earthquake: Broadband source process. *Geophysical Research Letters* **25**, 2691–2694 (1998).

46. Ammon, C. J., Kanamori, H., Lay, T. & Velasco, A. A. The 17 july 2006 java tsunami earthquake. *Geophysical Research Letters* **33** (2006).

47. Perrin, G., Rice, J. R. & Zheng, G. Self-healing slip pulse on a frictional surface. *Journal of the Mechanics and Physics of Solids* **43**, 1461–1495 (1995).

48. Obara, K. Phenomenology of deep slow earthquake family in southwest japan: Spatiotemporal characteristics and segmentation. *Journal of Geophysical Research: Solid Earth* **115** (2010).

49. Bletery, Q. & Nocquet, J.-M. Slip bursts during coalescence of slow slip events in cascadia. *Nature Communications* **11**, 1–6 (2020).

50. Nocquet, J.-M. *et al.* Supercycle at the ecuadorian subduction zone revealed after the 2016 pedernales earthquake. *Nature Geoscience* **10**, 145–149 (2017).

51. Villegas-Lanza, J. C. *et al.* Active tectonics of peru: Heterogeneous interseismic coupling along the nazca megathrust, rigid motion of the peruvian sliver, and subandean shortening accommodation. *Journal of Geophysical Research: Solid Earth* **121**, 7371–7394 (2016).

52. Radiguet, M. *et al.* Slow slip events and strain accumulation in the guerrero gap, mexico. *Journal of Geophysical Research: Solid Earth* **117** (2012).

53. Wallace, L. M. Slow slip events in new zealand. *Annual Review of Earth and Planetary Sciences* **48**, 175–203 (2020).

54. Klein, E. *et al.* Deep transient slow slip detected by survey gps in the region of atacama, chile. *Geophysical Research Letters* **45**, 12,263–12,273 (2018).

55. Liu, Y. Numerical simulations on megathrust rupture stabilized under strong dilatancy strengthening in slow slip region. *Geophysical Research Letters* **40**, 1311–1316 (2013).

56. Brodsky, E. E. & Mori, J. Creep events slip less than ordinary earthquakes. *Geophysical Research Letters* **34** (2007).

57. Obara, K., Hirose, H., Yamamizu, F. & Kasahara, K. Episodic slow slip events accompanied by non-volcanic tremors in southwest japan subduction zone. *Geophysical Research Letters* **31** (2004).

58. Romanowicz, B. Strike-slip earthquakes on quasi-vertical transcurrent faults: Inferences for general scaling relations. *Geophysical Research Letters* **19**, 481–484 (1992).

59. Kano, M. *et al.* Development of a slow earthquake database. *Seismological Research Letters* **89**, 1566–1575 (2018).

60. Liu, Y. & Rubin, A. M. Role of fault gouge dilatancy on aseismic deformation transients. *Journal of Geophysical Research: Solid Earth* **115** (2010).

61. Segall, P., Rubin, A. M., Bradley, A. M. & Rice, J. R. Dilatant strengthening as a mechanism for slow slip events. *Journal of Geophysical Research: Solid Earth* **115** (2010).

62. Yamashita, T. & Suzuki, T. Dynamic modeling of slow slip coupled with tremor. *Journal of Geophysical Research: Solid Earth* **116** (2011).

63. Liu, Y., McGuire, J. J. & Behn, M. D. Aseismic transient slip on the gofar transform fault, east pacific rise. *Proceedings of the National Academy of Sciences* **117**, 10188–10194 (2020).

64. Rousset, B. Months-long subduction slow slip events avoid the stress shadows of seismic asperities. *Journal of Geophysical Research: Solid Earth* **124**, 7227–7230 (2019).

65. Wech, A. G. & Creager, K. C. A continuum of stress, strength and slip in the cascadia subduction zone. *Nature Geoscience* **4**, 624–628 (2011).

66. Tan, Y. J. & Marsan, D. Connecting a broad spectrum of transient slip on the san andreas fault. *Science advances* **6**, eabb2489 (2020).

67. Rice, J. Heating and weakening of faults during earthquake slip. *Journal of Geophysical Research: Solid Earth* **111** (2006).

68. Bilek, S. L. & Lay, T. Rigidity variations with depth along interplate megathrust faults in subduction zones. *Nature* **400**, 443–446 (1999).

69. Sallarès, V. & Ranero, C. R. Upper-plate rigidity determines depth-varying rupture behaviour of megathrust earthquakes. *Nature* **576**, 96–101 (2019).

70. Ma, S. A self-consistent mechanism for slow dynamic deformation and tsunami generation for earthquakes in the shallow subduction zone. *Geophysical Research Letters* **39** (2012).

71. Corbi, F., Funiciello, F., Brizzi, S., Lallemand, S. & Rosenau, M. Control of asperities size and spacing on seismic behavior of subduction megathrusts. *Geophysical Research Letters* **44**, 8227–8235 (2017).

72. Dieterich, J. Applications of rate-and state-dependent friction to models of fault slip and earthquake occurrence. *Treat. Geophys.* **4**, 107–129 (2007).

73. Kato, N. A possible model for large preseismic slip on a deeper extension of a seismic rupture plane. *Earth and Planetary Science Letters* **216**, 17–25 (2003).

74. Dieterich, J. H. Modeling of rock friction: 1. experimental results and constitutive equations. *Journal of Geophysical Research: Solid Earth* **84**, 2161–2168 (1979).

75. Luo, Y., Ampuero, J., Galvez, P., Van den Ende, M. & Idini, B. Qdyn: a quasi-dynamic earthquake simulator (v1. 1). *Zenodo.(doi: 10.5281/zenodo. 322459)* (2017).

76. Ampuero, J.-P. Sem2dpack, a spectral element software for 2d seismic wave propagation and earthquake source dynamics, v2.3.8. *Zenodo* (2012).

77. Noda, H. & Lapusta, N. Stable creeping fault segments can become destructive as a result of dynamic weakening. *Nature* **493**, 518–521 (2013).

78. Viesca, R. C. & Garagash, D. I. Ubiquitous weakening of faults due to thermal pressurization. *Nature Geoscience* **8**, 875–879 (2015).

79. Freund, L. *Dynamic fracture mechanics* (Cambridge university press, 1998).

80. Rubin, A. & Ampuero, J. Earthquake nucleation on (aging) rate and state faults. *Journal of Geophysical Research: Solid Earth* **110** (2005).

81. Gabriel, A., Ampuero, J., Dalguer, L. & Mai, P. M. Source properties of dynamic rupture pulses with off-fault plasticity. *Journal of Geophysical Research: Solid Earth* **118**, 4117–4126 (2013).

82. Ida, Y. The maximum acceleration of seismic ground motion. *Bulletin of the Seismological Society of America* **63**, 959–968 (1973).

Acknowledgements This manuscript benefited from discussions with Jean-Paul Ampuero, M.P.A. van den Ende, Quentin Bletery, and Jean-Mathieu Nocquet. I thank Jean-Paul Ampuero and Frédéric Cappa in reviewing the early version of this manuscript. I am grateful to Jean-Paul Ampuero for his constructive comments and his suggestion of empirically estimating the average slip rate of the observed SSEs and to analyze the moment-duration scaling resulting from the model. This work was supported by the French government through the Investments in the Future project UCAJEDI (ANR-15-IDEX-01) managed by the French National Research Agency (ANR).

Correspondence Correspondence should be addressed to Huihui Weng (email: weng@geoazur.unice.fr).

Code availability The open-source softwares SEM3DPACK and QDYN used in the fill-dynamic and quasi-dynamic rupture simulations is available at https://github.com/jpampuero/sem2dpack and https://github.com/ydluo/qdyn.

Competing Interests The author declares that he has no competing interests.

Figure 1 Sketch of SSE and earthquake ruptures on subduction zone and stability conditions. (a) Sketch of subduction zone comprised of tsunamigenic, seismogenic, and SSE zones with finite widths. Elongated SSE (blue curves) and earthquake (red curves) ruptures start at the hypocenters, indicated by red stars. (b) Sketches of dissipated fracture energy and energy release rate of ruptures as functions of peak slip rate or rupture speed.

Figure 2 A continuum of rupture speeds predicted by theory. (a) Symbols represent rupture speed as a function of stress drop based on fully dynamic (stars) and quasi-dynamic (diamonds) simulations, with colour coded by critical slip rate (legend in (b)). v_s and σ are the S-wave speed and effective normal stress, respectively. (b) Comparison of rupture speeds between numerical simulations (stars and diamonds) and theoretical prediction (black curve). (c) Comparison of peak slip rates between numerical simulations (stars and diamonds) and theoretical prediction (black curve).

Figure 3 Non-steady ruptures due to along-strike heterogeneities. (a) Curves show the transition of rupture speeds from one steady state at segment 1 to another steady state at segment 2 based on fully dynamic (coloured curves) and quasi-dynamic (grey curves) simulations. The colour is coded by the steady rupture speed at segment 2. (b) Rupture arresting distances inside a barrier versus the peak slip rate before reaching the barrier, based on fully dynamic (coloured stars) and quasi-dynamic (grey diamonds) simulations. The colour is coded by the steady rupture speed before reaching the barrier. The inset shows the sketch of rupture propagation after reaching a barrier.

Figure 4 Scaling relation of SSEs and earthquakes. (a) Linear and cubic moment-duration scaling relations based on homogeneous (pink circles) and linear decay (green triangles) models. $\Delta\tau^{run}$ and v_r^{run} are the critical stress drop and rupture speed for steady SSEs (Methods A7). (b) Cubic scaling relations for different values of effective normal stress σ. The grey region marks a linear envelope scaling. (c) Symbols represent estimates of rupture speed versus peak slip rate of global SSEs and tsunami earthquakes (error bar indicates uncertainty when available; aspect ratios are larger than 2), compiled from refs[36,44–46,59]. Dashed curves mark the theoretical predictions assuming constant strength drops. (d) The scaling relation between normalized rupture speed and peak slip rate for global SSEs and tsunami earthquakes. The thick curve marks the theoretical prediction.

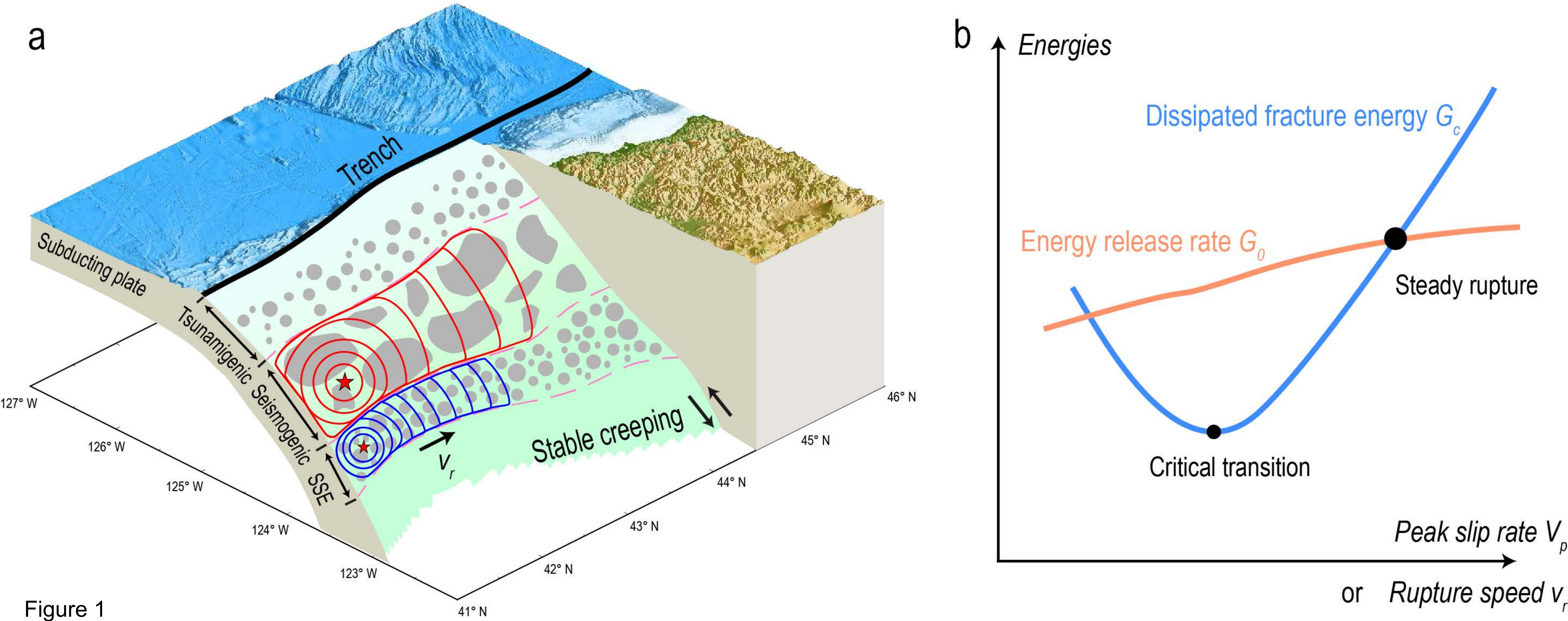
a
Trench
Subducting plate
Tsunamigenic
Seismogenic
SSE
Stable creeping
V_r
127° W
126° W
125° W
124° W
123° W
41° N
42° N
43° N
44° N
45° N
46° N
b
Energies
Dissipated fracture energy G_c
Energy release rate G_0
Steady rupture
Critical transition
Peak slip rate V_p
or Rupture speed v_r

Figure 1

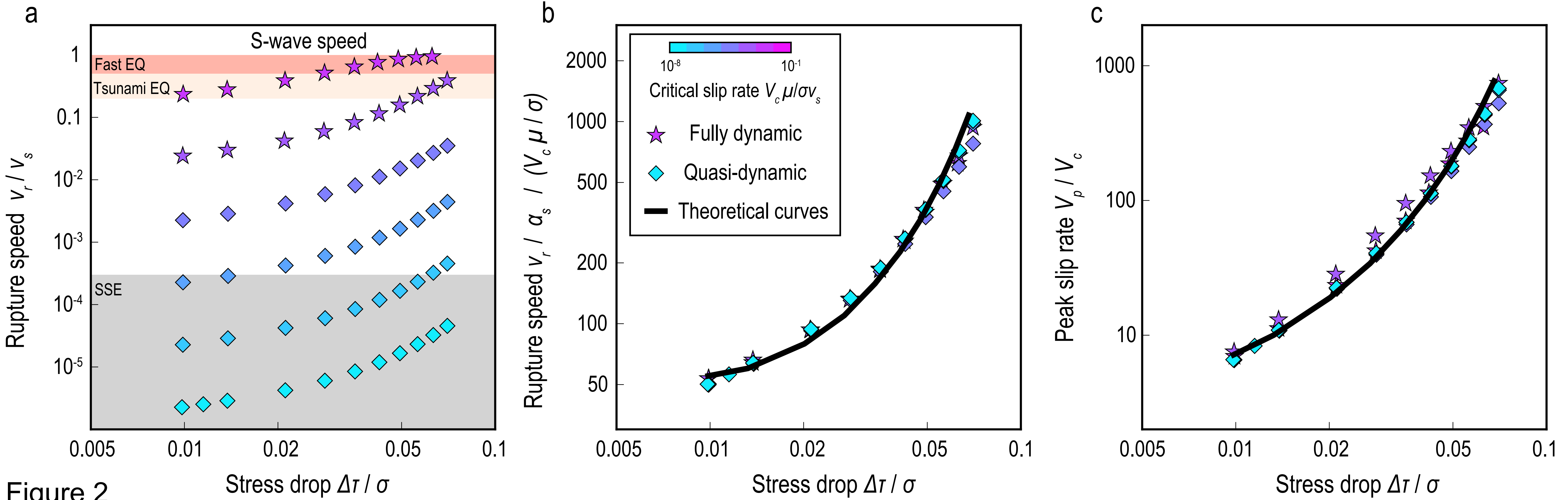

a
S-wave speed
Fast EQ
Tsunami EQ
SSE
Rupture speed v_r / v_s
Stress drop $\Delta\tau / \sigma$
b
Critical slip rate $V_c \mu / \sigma v_s$
Fully dynamic
Quasi-dynamic
Theoretical curves
Rupture speed $v_r / \alpha_s / (V_c \mu / \sigma)$
Stress drop $\Delta\tau / \sigma$
c
Peak slip rate V_p / V_c
Stress drop $\Delta\tau / \sigma$

Figure 2

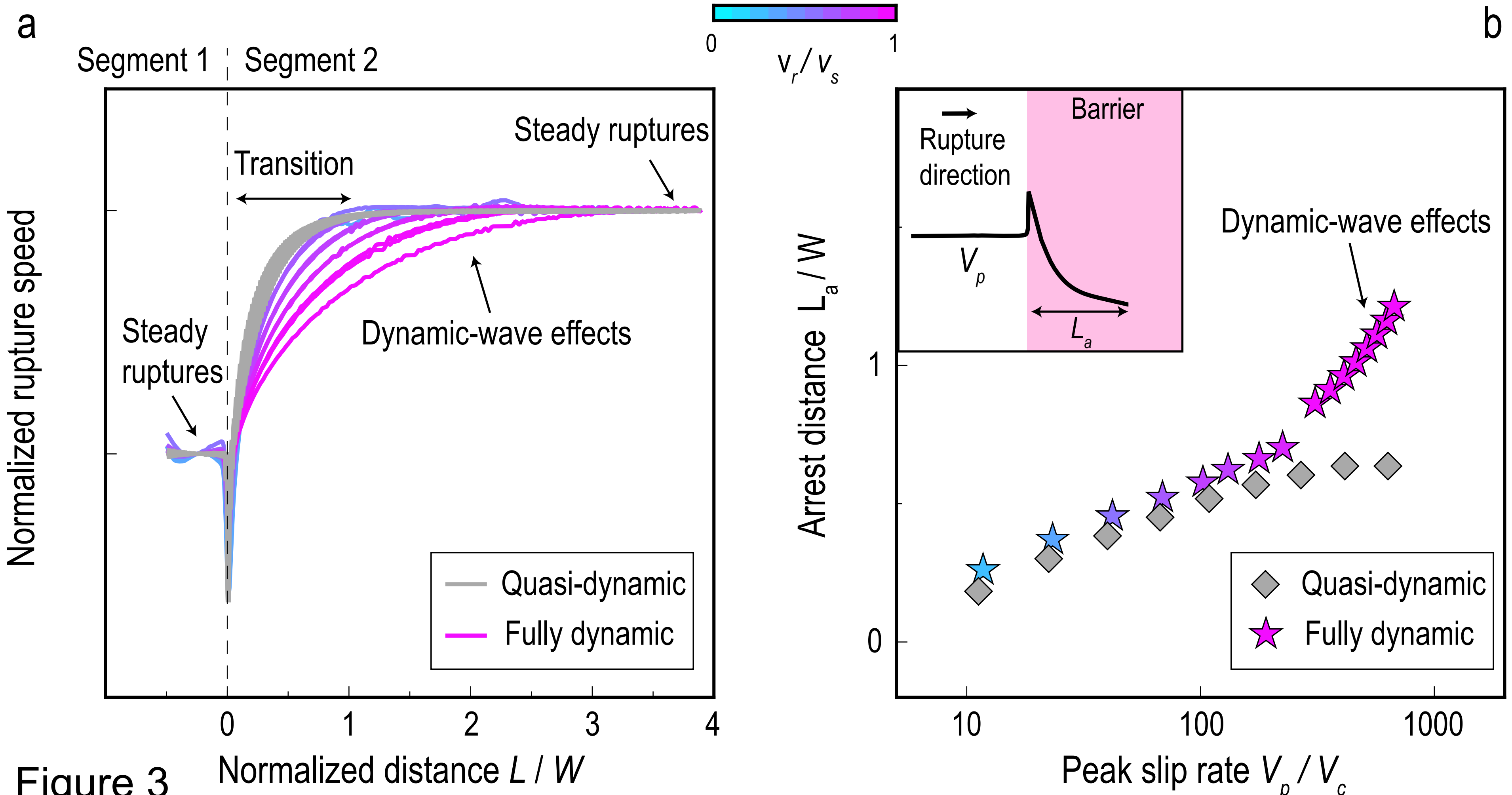
a
Segment 1
Segment 2
0
1
v_r / v_s
Steady ruptures
Transition
Steady ruptures
Dynamic-wave effects
Normalized rupture speed
Quasi-dynamic
Fully dynamic
0
1
2
3
4
Normalized distance L / W
b
Barrier
Rupture direction
V_p
L_a
Dynamic-wave effects
Arrest distance L_a / W
1
0
Quasi-dynamic
Fully dynamic
10
100
1000
Peak slip rate V_p / V_c

Figure 3

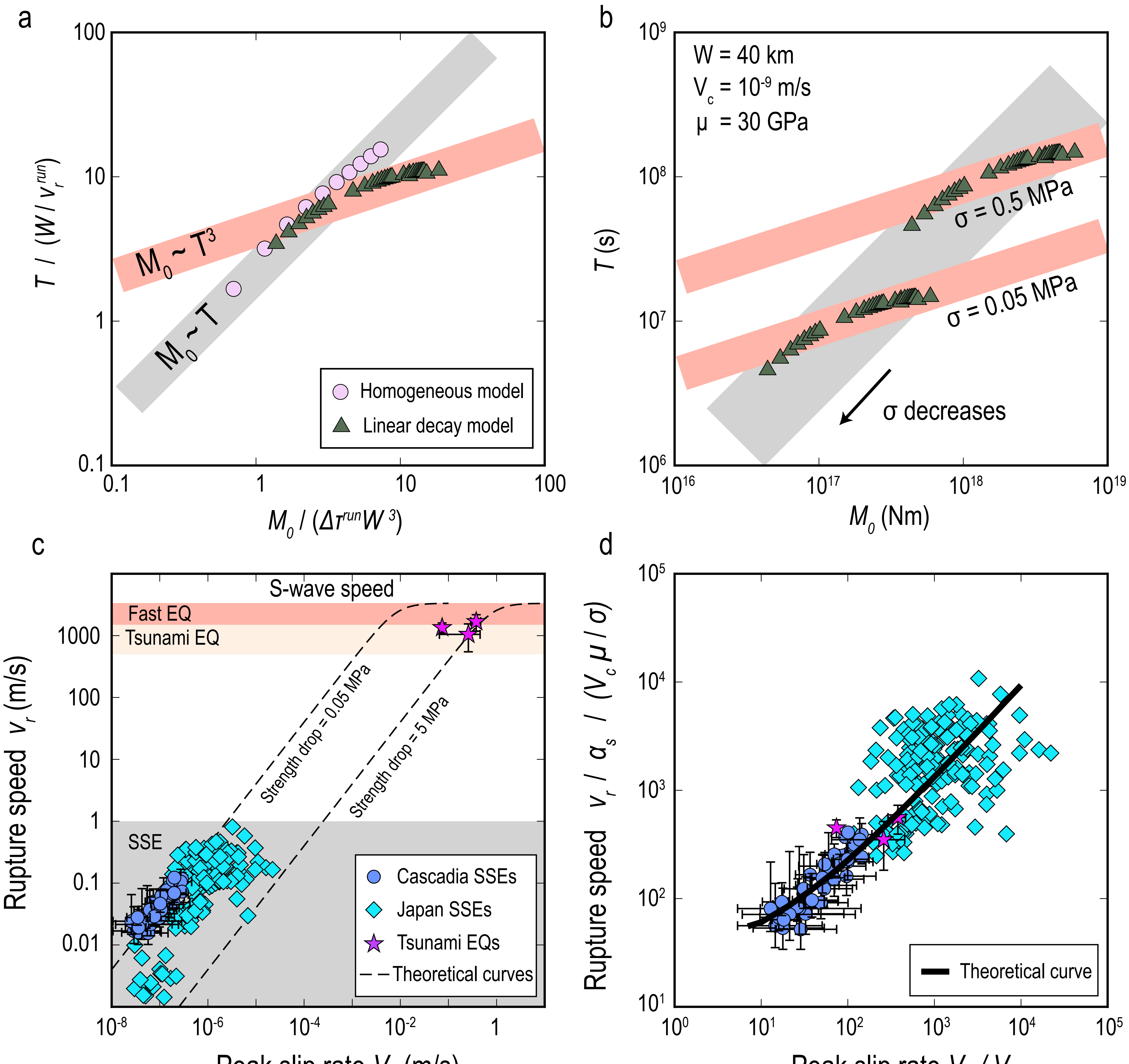
a
b
c
d
$M_0 \sim T^3$
$M_0 \sim T$
Homogeneous model
Linear decay model
T / (W / v_r^{run})
M_0 / ($\Delta\tau^{run} W^3$)
W = 40 km
$V_c = 10^{-9}$ m/s
μ = 30 GPa
σ = 0.5 MPa
σ = 0.05 MPa
σ decreases
T (s)
M_0 (Nm)
S-wave speed
Fast EQ
Tsunami EQ
SSE
Strength drop = 0.05 MPa
Strength drop = 5 MPa
Cascadia SSEs
Japan SSEs
Tsunami EQs
Theoretical curves
Rupture speed v_r (m/s)
Peak slip rate V_p (m/s)
Theoretical curve
Rupture speed v_r / α_s / ($V_c \mu / \sigma$)
Peak slip rate V_p / V_c

Figure 4

Slow slip events are regular earthquakes

Huihui Weng[1*]

[1]*Université Côte d'Azur, IRD, CNRS, Observatoire de la Côte d'Azur, Géoazur, 250 rue Albert Einstein, Sophia Antipolis, 06560 Valbonne, France*

Correspondence to Huihui Weng (email: weng@geoazur.unice.fr)

Contents

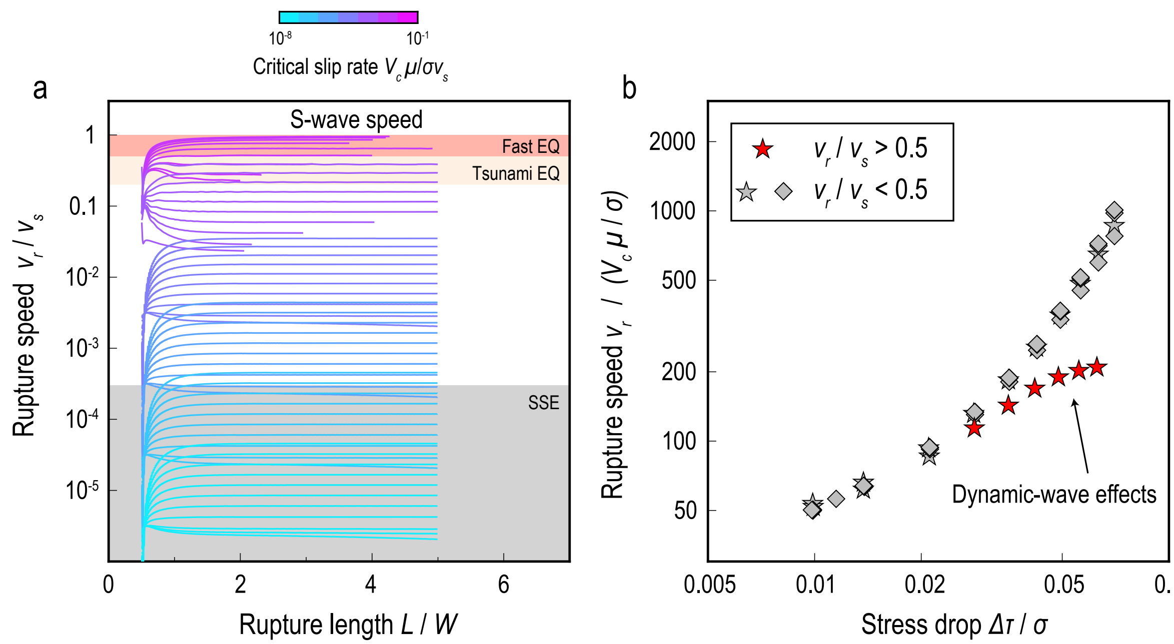

Figure S1: Rupture propagation of SSEs and earthquakes. (a) Coloured curves represent rupture speed as a function of normalized rupture distance based on fully dynamic and quasi-dynamic simulations (coloured curves coded by critical slip rate). (b) Normalized rupture speed (not accounting for the Lorentz contraction factor) versus normalized stress drop for simulated ruptures shown in the legend.

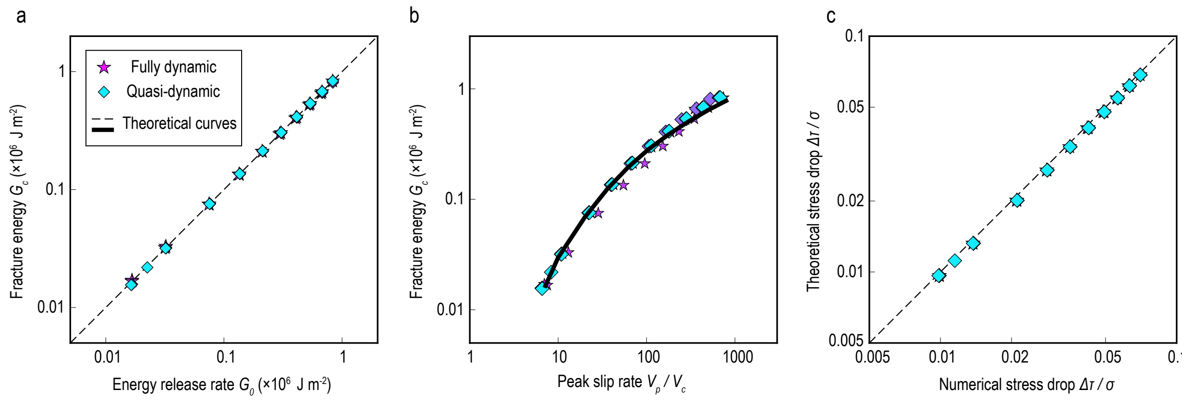

Figure S2: Energies of steady SSE and earthquake ruptures. (a) Symbols represent fracture energy and energy release rate numerically estimated from the fully dynamic and quasi-dynamic simulations (legend). The dashed line indicates the energy balance predicted by theory. (b) Fracture energy versus peak slip rate based on fully dynamic and quasi-dynamic simulations. The black curve is the theoretical prediction. (c) Comparison of stress drop between the numerical and theoretical estimates based on fully dynamic and quasi-dynamic simulations.

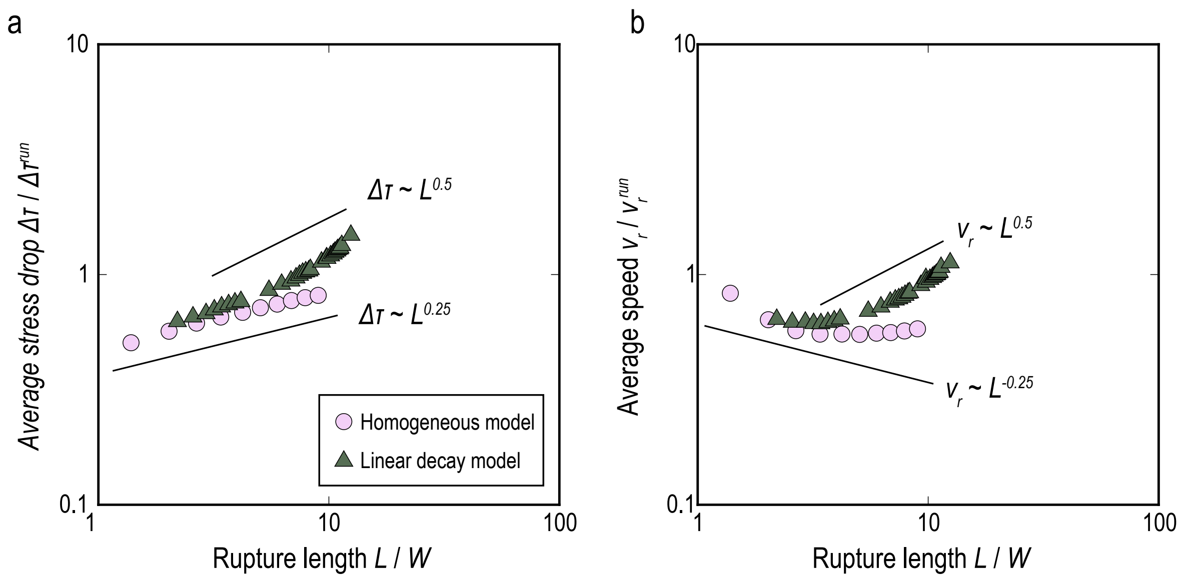

Figure S3: Scaling relations of stress drop and rupture speed. (a) Pink circles (homogeneous model) and green triangles (linear decay model) represent the scaling relation between stress drop and rupture length. (b) The scaling relation between rupture speed and rupture length.

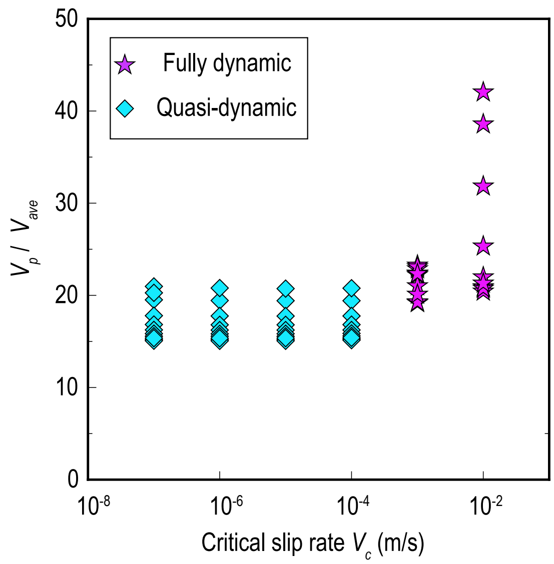

Figure S4: Empirical ratio between peak and average slip rates. Symbols represent the ratio of peak slip rate to average slip rate for various critical slip rates based on fully dynamic (stars) and quasi-dynamic (diamonds) simulations.

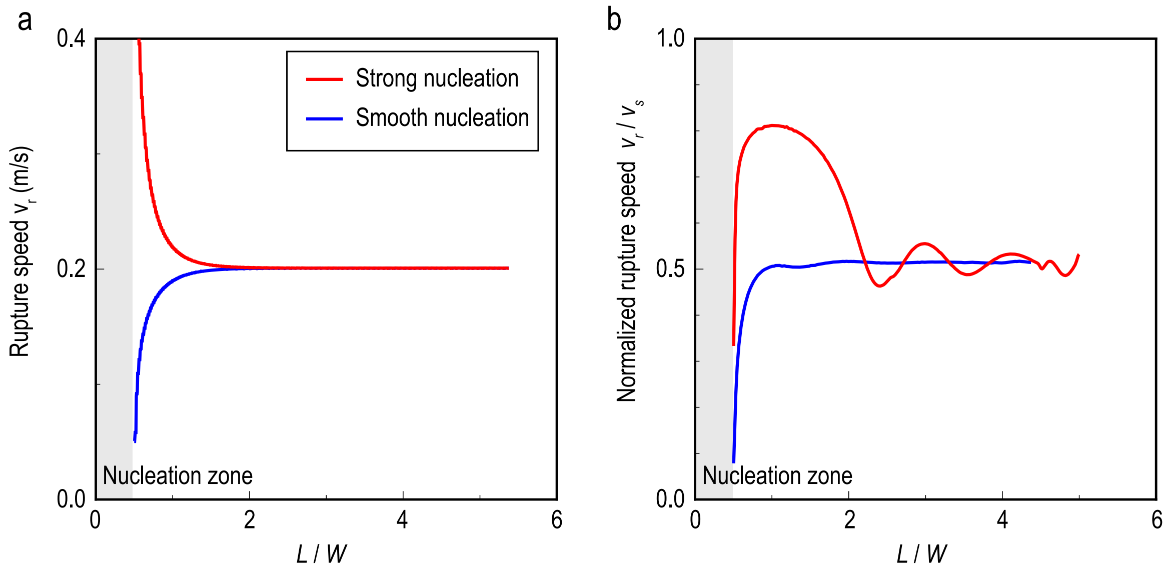

Figure S5: Effects of nucleation conditions on steady rupture propagation. (a) Rupture speeds as a function of normalized distance for two quasi-dynamic SSE simulations with different nucleation strategies: strong overstressed nucleation and smooth nucleation. The grey region marks the nucleation zone. (b) same as (a), but for fully dynamic earthquake simulations.

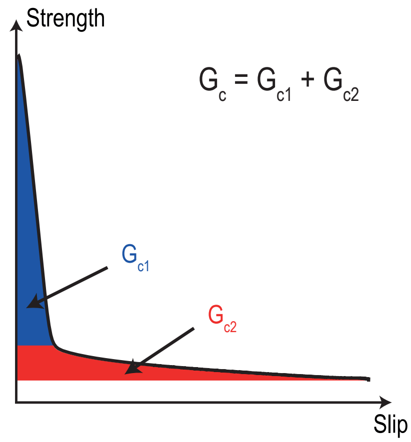

Figure S6: One example of fault strength evolution The evolution of fault strength as a function of fault slip governed by V-shape rate-and-state friction. The blue region marks the fracture energy caused by the first weakening stage. The red region marks the fracture energy caused by the second weakening stage.

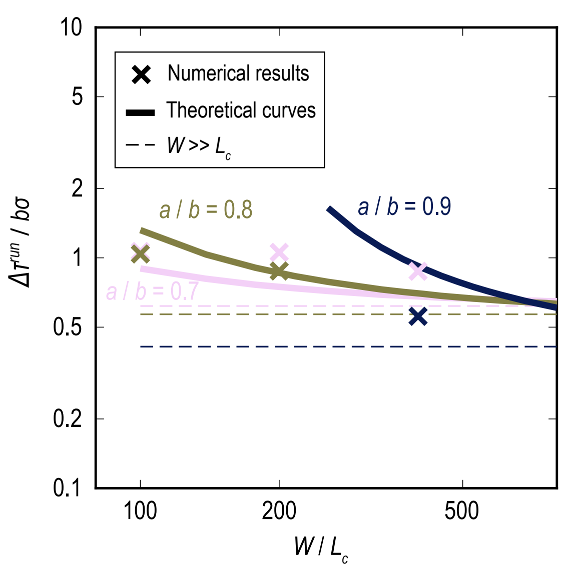

Figure S7: Dependence of critical stress drop for runaway ruptures The critical stress drop $\Delta\tau_{run}/b\sigma$ versus W/L_c for different values of a/b (colours), based on the numerical simulations (cross symbols) and the theoretical predictions (thick and dash curves).